Nanoscale

Accepted Manuscript

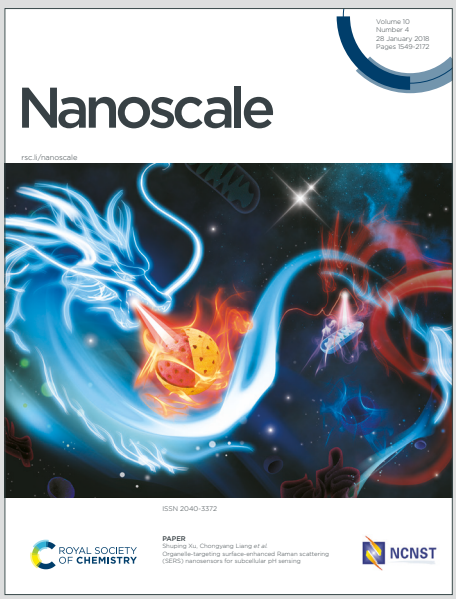

ROYAL SOCIETY OF CHEMISTRY

rsc.li/nanoscale

Nanoscale

PAPER

Ordered mesoporous carbon with binary CoFe atomic species for highly efficient oxygen reduction electrocatalysis

Received 00th January 20xx,
Accepted 00th January 20xx

DOI: 10.1039/x0xx00000x

Fengying Pan,‡[,a] Ziyan Shen,‡[,a] Xianjun Cao,[a] Yuxia Zhang,[b] Cheng Gong,[a] Jinhu Wu,[a] Jinqiang Zhang,*[,c] Hao Liu,*[,c] Xiaowei Li*[,d] and Yufei Zhao*[,a,c]

The exploration of powerful, efficient and precious metal free electrocatalysts for facilitating the sluggish kinetics of oxygen reduction reaction (ORR) is a crucial endeavor in the development and application of energy conversion and storage devices. Herein, we have rationally designed and synthesized bimetallic CoFe species consisting of CoFe nanoparticles and atomically dispersed dual atoms anchored on ordered mesoporous carbon matrix (CoFe/NC) as highly efficient ORR electrocatalysts. The pyrolyzed temperature for CoFe/NC plays a vital role in regulating the morphology and composition of both carbon matrix and CoFe species. The optimized CoFe/NC-750 exhibits a favorable ORR performance in 0.1 M KOH with a high half-wave potential ($E_{1/2}$) of 0.87 V vs. RHE, excellent tolerance to methanol and remarkable durability (no obvious decay in $E_{1/2}$ after 3000 cycles), all of which are superior to the performance of commercial Pt/C. Experimental measurements and density functional theory (DFT) calculations manifest that the improved ORR performance of CoFe/NC-750 is mainly attributed to the electronic structure of atomically dispersed Fe active sites modulated by the surrounding CoFe alloys and Co single atoms, which accelerates the dissociation and reduction of intermediates OH* and promotes the ORR process.

1 Introduction

Proton-exchange membrane fuel cell and metal-air batteries have aroused widespread interest in providing clean energy as a promising alternative to fossil fuels for remarkable energy conversion efficiency, high mass energy density as well as near-zero emissions.[1] Their inherent defects of sluggish cathode oxygen reduction reaction (ORR) kinetics, coupled with exorbitant cost, scarcity and poor durability of platinum-group-metal with excellent ORR catalytic performance, have caused great resistance to widespread commercial application.[2-5] For decades, massive efforts have been made to explore the non-precious metal catalysts as candidates to replace the Pt-based composites for ORR such as metal oxides, nitrides, carbides, hydroxides, sulfides.[6, 7] Nevertheless, the utilization efficiency of metal atoms is relatively low and the catalytic mechanism of such electrocatalysts have been limited due to their heterogeneity properties.

Recently, nitrogen stabilized transition metal species (TM-Nx) supported by carbon substrates have been proved to be one of the most promising alternatives owing to their maximized metal atom utilization and tunable electronic properties.[8-11] Among them, Fe-N-C electrocatalysts have exhibited high catalytic activity with the Fe-N coordination bonds as ORR active sites.[12, 13] It has been demonstrated that their ORR activity can be further boosted by altering the electronic structure, which highly affect the binding energy with the ORR intermediates.[14] For instance, the introduction of other types of heteroatoms (e.g., S, P, B) can tune and enhance the kinetic activity of catalytic sites (M-S_1N_3, P/Fe-N-C) by regulating the electron-withdrawing/donating properties.[15, 16] Bimetallic sites with incorporating another metal species endowed with synergistic properties have great potential to accelerate ORR kinetics. The intrinsic ORR activity of the active metal species of SACs follows the order of Fe>Co>Cu>Mn>Ni.[17-19] Therefore, incorporating Co species into Fe-N-C electrocatalysts forming adjacent metal atoms, greatly improves the structural adjustability. The chemical interaction between Fe and Co atoms leads to unique electronic structure and optimized ORR performance. For instance, FeN3-CoN3 active sites highly promote the cleavage of O-O bonds by bridge-cis adsorption of O-containing intermediates in the ORR process. In addition, the insertion of atomic clusters into atomically dispersed M-N-C substrates (e.g., Fe_{AC}@Fe_{SA}-N-C, Fe-ACSA@NC, Co-ACSA@NC, Ni-ACSA@NC) inspired the electron redistribution between the metal centers in M-N-C and carbon support, regulating the bonding length of M-N to promote the desorption of intermediates during ORR process.[20-22] Furthermore, the introduction of nanoparticles nearby the atomically dispersed

[a] Joint International Laboratory on Environmental and Energy Frontier Materials, School of Environmental and Chemical Engineering, Shanghai University, Shanghai 200444, P. R. China.
[b] School of Materials Science and Engineering, Shijiazhuang Tiedao University, Shijiazhuang 050043, P. R. China.
[c] Centre for Clean Energy Technology, Faculty of Science, University of Technology Sydney, Broadway, Sydney, NSW 2007, Australia
[d] School of Environmental and Chemical Engineering, Organic Compound Pollution Control Engineering, Ministry of Education, Shanghai University, Shanghai 200444, P. R. China.
† Electronic Supplementary Information (ESI) available. See DOI: 10.1039/x0xx00000x
‡ Fengying Pan and Ziyan Shen made equal contributions to this work.

M-N-C (M/M-N_X) is also promising to optimize the ORR performance[23-25]. For instance, M/M-N_X composite sites (e.g., M/FeCo-SAs-N-C, FeN_3/Fe NPs) enhanced the oxygen adsorption capability and prolonged the length of the O-O bond, making the O-O bond easily fractured and thereby enhancing the ORR catalytic activity.[26, 27] Apart from collaborating with M-N-C, the incorporated heteroatoms, clusters or nanoparticles may also provide additional active sites or protect the M-N-C active site from poisoning,[28, 29] further boosting the catalytic activity and stability. However, in-depth understanding of the interaction between the active sites and reactants to accelerate the ORR kinetics is still heavily hampered by the heterogeneity of the structure and composition of the electrocatalysts,[6, 27] and establishing a definitive correlation between the atomic structure and the ORR catalytic performance remains a challenge.[30, 31]

Herein, we designed a template assisted method to prepare highly efficient ORR electrocatalysts composing of an ordered mesoporous carbon and bimetallic CoFe species. The pyrolyzed temperature for CoFe/NC highly regulates the properties of carbon matrix and CoFe species. The optimized CoFe/NC-750 exhibits ordered porous architecture, and coexistence of atomically dispersed Co/Fe atoms and CoFe alloys, which ensure the efficient mass transport and modulate active sites for ORR. As a result, CoFe/NC-750 have exhibited excellent ORR performance in alkaline condition with a high $E_{1/2}$, excellent tolerance to methanol and superior durability, outperforming those of commercial Pt/C and other prepared comparison samples. The boosted ORR performance of CoFe/NC-750 may mainly contribute to the active sites of atomically dispersed Fe species modulated by the surrounding Co atoms and CoFe alloys, which lowers the energy barrier in the rate-determining step ($OH^* \rightarrow OH^-$), thus accelerating the ORR process.

2 Results and Discussion

2.1 Fabrication and characterization

The synthesis procedure of CoFe/NC-750 is depicted in Fig. 1a. The hard template SBA-15 has been prepared based on the reported methods.[32] Then the metal-organic ligand complexes were in-situ formed in the pores of SBA-15 with incorporating organic ligand 2-methylimidazole, Co^{2+} and Fe^{3+} nodes. The bimetallic CoFe species (CoFe nanoparticles and atomically dispersed Co/Fe atoms) anchored on mesoporous carbon matrix (CoFe/NC-750) has been achieved after 750 °C pyrolysis, hard template removal, and acid treatment for removing the accessible metal nanoparticles.

The ordered mesoporous structure of CoFe/NC-750 derived from the reverse replication of SBA-15 (SEM image in Fig. S1) has been confirmed by scanning electron microscopy (SEM) and transmission electron microscopy (TEM) images (Fig. S2). The high angle annular dark-field scanning transmission electron microscopy (HAADF-STEM) image in Fig. 1b has further shown that CoFe/NC-750 inherits the rod-like structure with nanoparticles scattered on its surface. The high resolution HAADF-STEM image in Fig. 1c reveals the presence of well crystalized nanoparticle structure with the lattice fringes of 0.202 nm, corresponding to the (110) facet of the bcc CoFe alloy.[33] Meanwhile, numerous bright dots have been observed on the carbon support in Fig. 1d, attributing to the atomically dispersed Co or Fe species. Thus, we have successfully prepared the CoFe nanoparticles and CoFe atomically dispersed atoms co-existing on the carbon matrix. The energy dispersion spectrum (EDS) element mapping (Fig. 1e-h) combined with the electron energy loss spectroscopy (EELS) elemental mapping (Fig. S3) further validate the uniform distribution of C, N, Co, Fe elements and the presence of nano-aggregated CoFe metal alloy nanoparticles. The Co and Fe loading on the carbon matrix in CoFe/NC-750 are 5.42 wt% and 1.80 wt% respectively, derived from inductively coupled plasma optical emission spectrometry (ICP-OES) measurement.

CoFe/NCs pyrolyzed at different temperature have also been prepared as comparison materials to investigate the critical role of temperature, denoted as CoFe/NC-T (T= 700 °C, 750 °C, 800 °C, 850 °C). As shown in Fig. 2a, at a lower temperature of 700 °C, it is obvious to observe the nanoparticles due to their fast formation properties. With the increase of temperature to 750 ◦C, the co-existence of small nanoparticles and dual atoms have been observed (Fig. 1b-d). When the temperature further increased to 800 °C, the carbon surface becomes much rougher (Fig. 2a). Many carbon nanotubes (CNTs) formed due to the catalytic properties of CoFe alloys at higher temperature. More organic ligand 2-methylimidazole served as the C source for growth of CNTs in the presence of metallic alloys at temperature of 850 °C (forming interconnected CNTs), and eventually destroy the original ordered structure of CMK-3. Moreover, much less nanoparticles have been observed for CoFe/NC-800 and CoFe/NC-850, which may attribute to the quick movement of metal species at high temperature, reducing the aggregated properties. The above phenomena indicates that the temperature indeed plays a significant role for the unique morphology and composition. The results of N_2 adsorption/desorption isotherms in Fig. S5 reveal that CoFe/NC-750 with an ordered mesoporous structure and small nanoparticles has exhibited the largest specific surface area of 2109.3 $m^2 g^{-1}$ among all prepared CoFe/NCs samples (566.1 $m^2 g^{-1}$ for CoFe/NC-700, 1487.2 $m^2 g^{-1}$ for CoFe/NC-800 and 874.6 $m^2 g^{-1}$ for CoFe/NC-850), which is favorable for mass transport, more exposed active sites and the adsorption/desorption of intermediates.[34]

The composition and crystal structure of CoFe/NCs have been investigated by X-ray diffraction (XRD). As displayed in Fig. 2b, the dominant diffraction peak at 26° for all samples correspond to the (002) planes of graphitic carbon (JCPDS No.41-1487).[12] Two sharp peaks at around 45° have been observed for CoFe/NCs-700, belonging to the (111) plane of Co and (110) plane of CoFe alloy (JCPDS No.49-1568).[33] CoFe/NC-750 has exhibited one peak at 45°, corresponding to (110) plane of CoFe alloy. In contrast, the peaks for metallic species are almost indiscernible for both CoFe/NC-800 and CoFe/NC-850. The XRD results are consistent with the TEM images in Fig. 2a. Fig. 2c shows the Raman spectra of CoFe/NC, and the characteristic peaks around 1345 and 1585 cm^{-1} are dictated to the D-band of

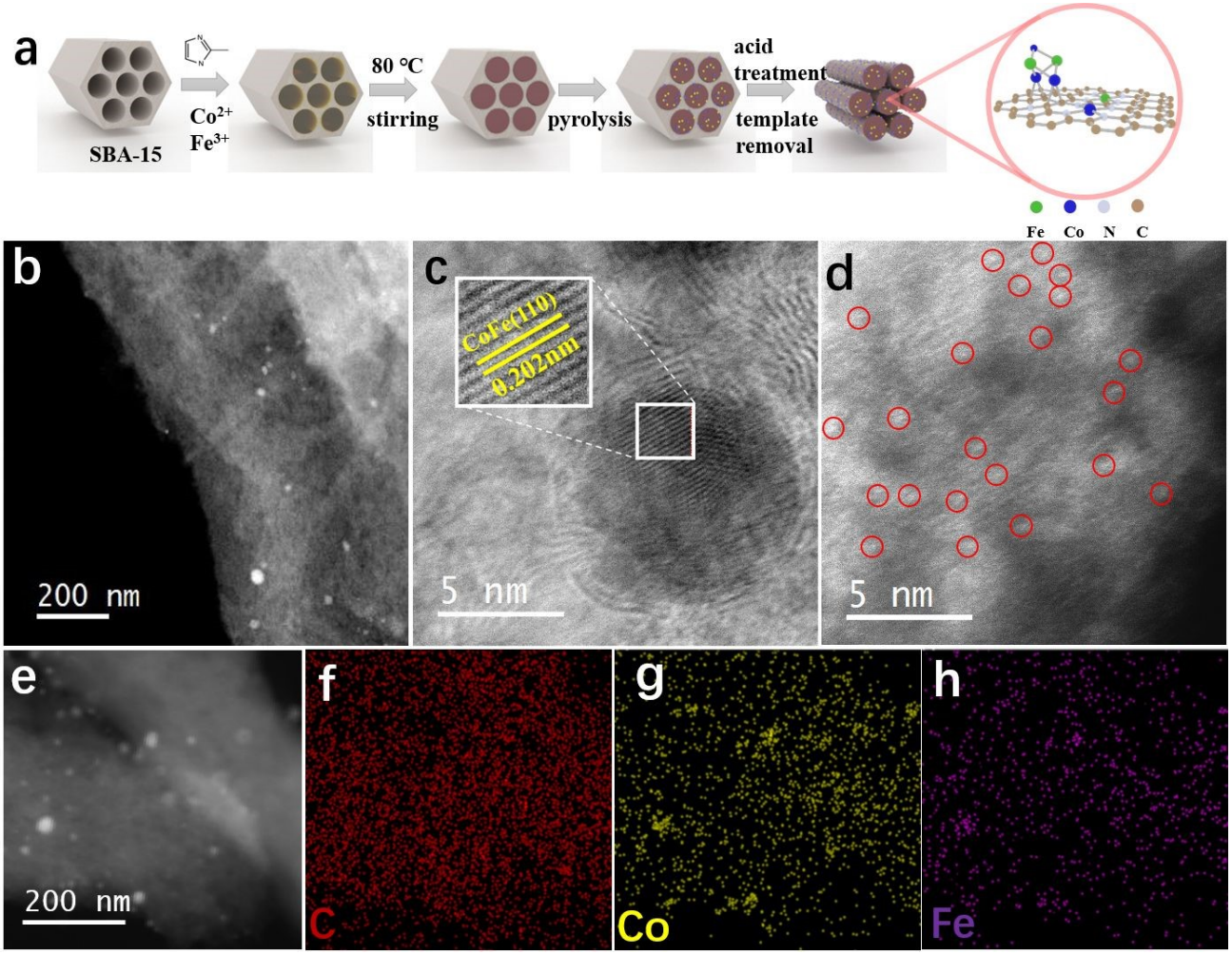

Fig. 1 Synthesis procedure schematic and morphology characterizations of the catalysts. (a) Synthetic schematic of CoFe/NC. (b-d) HAADF-STEM, high-resolution TEM and HAADF-STEM images of CoFe/NC-750. (e-h) Elemental mapping of CoFe/NC-750.

sp^3 defects and the G-band of sp^2 graphite carbon, respectively.[35, 36] CoFe/NC-750 exhibits the I_D/I_G intensity ratio of 0.96, which is a little higher than those of CoFe/NC-700 (0.93), CoFe/NC-800 (0.94) and CoFe/NC-850 (0.90). The increased I_D/I_G suggests the carbon lattice of CoFe/NC-750 possess more defects, which may provide additional active sites for ORR process.

The chemical and electronic states of as-prepared catalysts have been investigated by X-ray photoelectron spectroscopy (XPS) measurement. The XPS survey spectra in Fig. S6 show that all CoFe/NCs samples are composed of C, N, O, Fe and Co elements. The high-resolution N 1s segments of CoFe/NCs shown in Fig. 2d were deconvoluted into five peaks centered at approximately ~398, ~399, ~400, ~401 and ~402 eV, which are attributed to pyridinic N, metal-coordinated nitrogen (M–N), pyrrolic N, graphitic N and oxidized N, respectively, revealing the successful incorporation of N doping in CoFe/NC.[37, 38] The presence of M-N reveals the coordination of N atom with Fe or Co atom.[39] Moreover, the intensities of M-N peaks change significantly with the temperature. The CoFe/NC-750, CoFe/NC-800 and CoFe/NC-850 have exhibited much higher peak intensity compared to that of CoFe/NC-700, indicating much more Co/Fe species stabilized by N atoms with increasing the temperature, which is consistent with the TEM/XRD results that metal species move faster along the temperature changing from the particles to single atoms eventually.[40] Analogously, the peak intensity of graphitic N exhibits similar trend to that of M-N, indicating high temperature in favor of the formation of graphitic N. The high-resolution Co 2p spectra of CoFe/NC-700 and CoFe/NC-750 (Fig. 2e) have shown two distinct peaks, belonging to Co $2p_{3/2}$ and Co $2p_{1/2}$. These peaks can be further deconvolved into four pairs of peaks located at ~778/~793 eV, ~781/~796 eV, ~783/~799 eV, and ~786/~802 eV, corresponding to Co $2p_{3/2}$ and Co $2p_{1/2}$ of metallic Co (Co^0), Co^{3+}, Co^{2+} and the satellite peaks, respectively,[41] confirming the coexistence of atomic and metallic states of Co species in both CoFe/NC-700 and CoFe/NC-750. Moreover, the peak intensity of metallic Co decreased from CoFe/NC-700 to CoFe/NC-750. There is no corresponding peak of Co^0 observed in either CoFe/NC-800 or CoFe/NC-850, further demonstrating the transition from metal state (Co^0) to atomic state (Co^{3+}/Co^{2+}) at high temperature. The results of high-resolution Fe 2p in Fig. 2f show similar trend to that of Co 2p results, revealing the coexistence of the metallic (~707/~720 eV) and atomic state of Fe (Fe^{2+}(~711/~722 eV) and Fe^{3+}(~715/~728 eV)) in CoFe/NC-700 and CoFe/NC-750,[42] and merely atomic states of Fe in

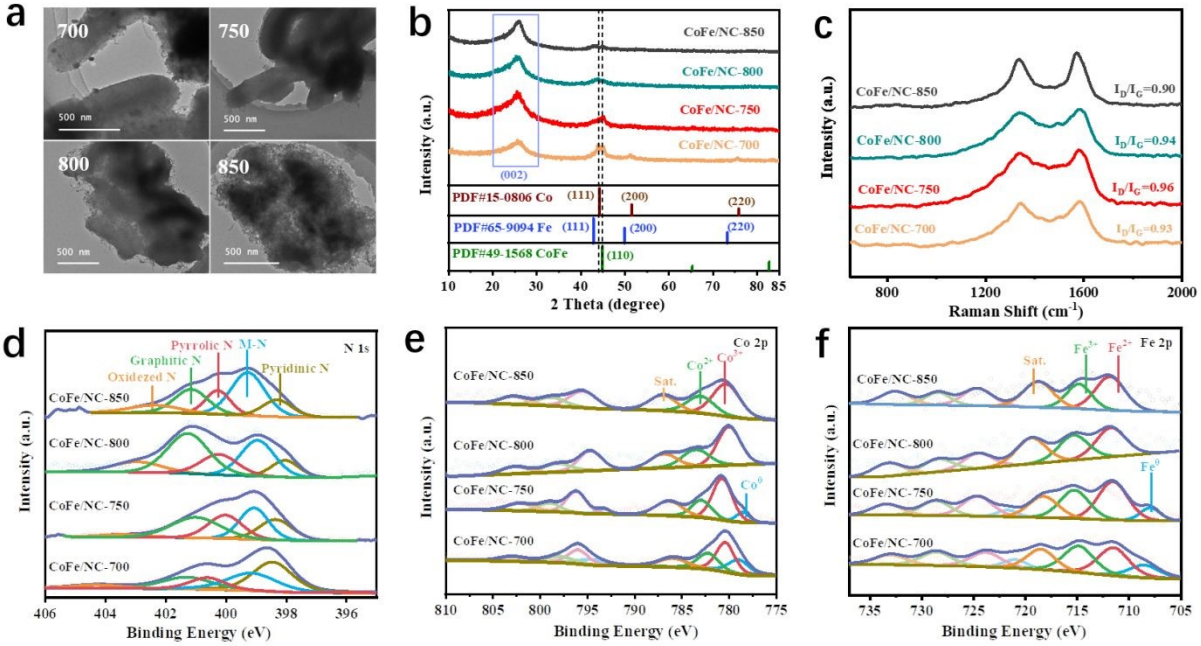

Fig. 1 Structural characterizations of the catalysts. (a) TEM images of CoFe/NC-T (T=700, 750, 800, 850 ℃). (b-c) XRD patterns and Raman spectra of CoFe/NC-T. Deconvoluted (d) N 1s, (e) Co 2p and (f) Fe 2p XPS spectra of CoFe/NC-T.

CoFe/NC-800 and CoFe/NC-850. The above results suggest that the temperature play an important role in promoting the transformation of metallic species into atomically dispersed metal species during CoFe preparation, which has a great influence on the morphology and composition of CoFe species and thus on the ORR catalytic capability.

2.2 ORR electrocatalytic performance

The electrocatalytic ORR performance of the as-prepared materials were critically investigated by linear sweep voltammetry (LSV) using a glassy rotating disk electrode (RDE) in O_2-saturated 0.1 M KOH solution with a rotation speed of 1600 rpm. As depicted in Fig. 3a, 3b, and Fig. S7, CoFe/NC-750 displays high E_{onset} and $E_{1/2}$ of 1.02V and 0.87 V vs. RHE, respectively, which are much better than those of Pt/C (E_{onset}=0.98V and $E_{1/2}$=0.86V) and CoFe/NCs (E_{onset}=0.97 V, 0.96 V, 0.95 V for CoFe/NC-700, CoFe/NC-800, CoFe/NC-850 and $E_{1/2}$=0.84 V, 0.85 V, 0.84 V for CoFe/NC-700, CoFe/NC-800, CoFe/NC-850, respectively). Meanwhile, the kinetic current density (J_K) of CoFe/NC-750 is 8.76 mA cm^{-2} at potential of 0.85 V vs. RHE and Tafel slope is 83 mV dec^{-1}, which is superior to the comparison samples (J_K =3.85 mA cm^{-2}, 5.32 mA cm^{-2}, 4.07 mA cm^{-2}, 5.3 mA cm^{-2} for CoFe/NC-700, CoFe/NC-800, CoFe/NC-850, Pt/C, and Tafel slope=103 mV dec^{-1}, 93 mV dec^{-1}, 95 mV dec^{-1}, 90 mV dec^{-1} for CoFe/NC-700, CoFe/NC-800, CoFe/NC-850, Pt/C, respectively). The above results demonstrate the enhanced electrocatalytic ORR activity and improved kinetics for CoFe/NC-750, ascribing to the ordered mesoporous structure promoting mass/charge transfer, and CoFe species offering ORR active sites. The LSV curves of CoFe/NC-750 were achieved at the speed range of 400 to 2025 rpm and the corresponding Koutechy-Levich (K-L) plots are shown in Fig. 3c. The approximately parallel fitting line properties (Fig. 3c, inset) manifest the first-order ORR kinetics of CoFe/NC-750.[43, 44] Moreover, the electron transfer number and hydrogen peroxide (H_2O_2) yield of CoFe/NC-750 during ORR were scrutinized by rotating ring-disk electrode (RRDE) tests. The results in Fig. 3d show that the electron transfer number is close to 4, and the H_2O_2 yield is lower than 4% throughout the whole potential window, confirming the four-electron ORR pathway of CoFe/NC-750. Compelling methanol tolerance of CoFe/NC-750 was investigated by adding methanol to the electrolyte during chronoamperometry measurement, and only less than 3% current attenuation has been observed, demonstrating the intrinsic methanol tolerance capability. In contrast, a significant decay for commercial Pt/C has been observed under the same condition (Fig. 3e). The durability of CoFe/NC-750 was assessed by the accelerated cyclic voltammetry test (ADT) and chronoamperometric test. The results in Fig. 3f show the LSV curves before and after ADT of 3000 cycles, manifesting slightly deviation of LSV curves and no obvious decay in $E_{1/2}$, which reveals the excellent ORR stability of CoFe/NC-750. In addition, the chronoamperometric result in Fig. S8 shows that the current density of CoFe/NC-750 maintains 99.9% of the initial value after 30,000s, further demonstrating the excellent stability properties during ORR process.

The superior ORR catalytic performance of CoFe/NC-750 over CoFe/NCs achieved at other temperature suggests that the ordered mesoporous structure and CoFe species play essential roles. We further prepared single metal species-based materials through the same synthesis procedure, Co/NC-750 and Fe/NC-750, to investigate the advantages of bimetallic species compared with single metallic species in improving ORR activity.

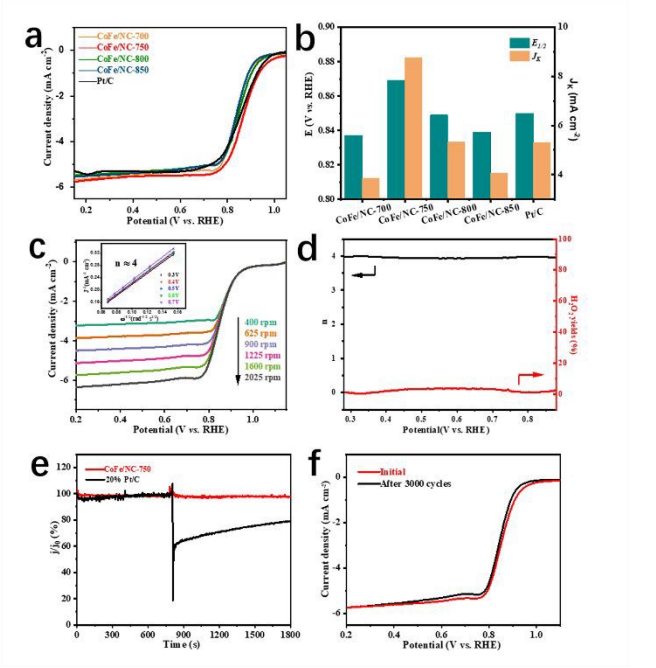

Fig. 2 Electrocatalytic ORR performance of the catalysts. (a) LSV polarization curves of CoFe/NC-T (T=700, 750, 800, 850 ℃) and Pt/C in O_2-saturated 0.1 M KOH solution with a rotation rate of 1600 rpm. (b) The comparison of $E_{1/2}$ and J_K at 0.85 V of CoFe/NC-T and Pt/C. (c) LSV curves of CoFe/NC-750 at different rotation rates (inset: corresponding K–L plot). (d) electron transfer number and H_2O_2 yield of CoFe/NC-750 from RRDE measurement. (e) chronoamperometric measurements of a methanol crossover test with CoFe/NC-750 and Pt/C. (f) Stability result for CoFe/NC-750.

The SEM images in Fig. S9a, S9b show that Co/NC-750 and Fe/NC-750 maintain the rod-like morphology similar to that of CoFe/NC-750. The structure properties of these materials are further characterized by XRD and Raman measurements. As illustrated in Fig. 4a, the XRD patterns of Co/NC-750 and Fe/NC-750 exhibit dominant characteristic peaks of graphitic carbon (002) plane at around 26°. No obvious peaks related to metallic Co or Fe species have been observed for Co/NC-750 and Fe/NC-750, which is a different phenomenon from that of CoFe/NC-750, indicating the solely metallic Co or Fe species may be easily removed by acidic treatment. The Raman spectra in Fig. 4b shows higher I_D/I_G intensity ratio of CoFe/NC-750, compared to Co/NC-750 and Fe/NC-750. Furthermore, N_2 adsorption/desorption isotherms results (Fig. S5, S9c and S9d) reveal CoFe/NC-750 possess higher BET surface area in comparison with Co/NC-750 and Fe/NC-750, contributing to exposure more active sites and the increased ORR kinetic activity. The ORR test results in Fig. 4c,4d and Fig. S10 reveal that CoFe/NC-750 delivers superior E_{onset}, $E_{1/2}$ and J_K to those of Co/NC-750 and Fe/NC-750, indicating that the synergistic effect of Co and Fe species contributed to the enhanced electrocatalytic ORR activity. In addition, as shown in Fig. S10, CoFe/NC-750 exhibits the smallest Tafel slope (83 mV dec^{-1}) compared to Co/NC-750 and Fe/NC-750, further demonstrating faster ORR kinetics of CoFe/NC-750 originating from the presence of bimetallic species.[44, 45]

2.3 DFT

DFT calculations were performed to understand the electronic structure and catalytic processes of the as-prepared CoFe/NC-750, further to elucidate the prominent ORR activity. We have constructed two models, CoFe/NC with CoFe alloys and dual atom sites and CoFe-dual atoms/NC with CoFe merely dual atom sites (Fig. 5a and Fig. S11a). As demonstrated in Fig. 5a, CoFe/NC-750 delivers a 4-electron pathway of the ORR process, thus the optimized configurations of the OOH*, O*, and OH* intermediates have been investigated. The Gibbs free energy diagram in Fig. 5b show that the final step of OH* reduction is the rate-determining step (RDS) for both CoFe-dual atoms/NC and CoFe/NC. CoFe/NC has exhibited a lower energy barrier of -0.526 eV for OH* reduction compared to that of CoFe-dual atoms/NC (-0.477 eV), demonstrating that CoFe/NC is more favorable for ORR process, which may originate from the electronic structure regulation of Fe single atom sites from the CoFe nanoparticles. We further employ the Fe atoms from the alloys as the active sites for OH* adsorption. The results in Fig. S11b show the energy barrier of the RDS has been increased, indicating that the CoFe nanoparticles in CoFe/NC are promoters rather than the catalytic active sites to boost the ORR process. Furthermore, the projected density of states (PDOS) of the active sites Fe atoms in CoFe-dual atoms/NC and CoFe/NC are illustrated in Fig. 5c. The calculated d-band center (ε_d) of Fe atoms (-2.012 eV) in CoFe/NC is slightly lower than that of CoFe-dual atoms/NC (-1.970 eV), promoting the dissociation of OH* and thus accelerating the ORR process. This further demonstrates that the incorporation of the CoFe nanoparticles modulates the electronic structure of Fe active sites for highly efficient ORR.

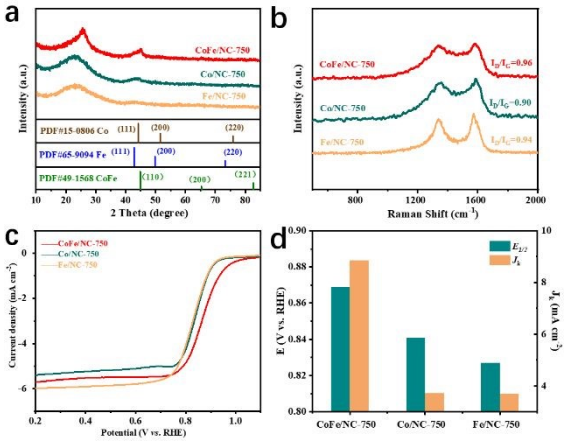

Fig. 3 (a-b) XRD patterns and Raman spectra of CoFe/NC-750, Co/NC-750 and Fe/NC-750. (c-b) LSV polarization curves and comparison of $E_{1/2}$ and J_K at 0.85 V of CoFe/NC-750, Co/NC-750 and Fe/NC-750.

3 Conclusions

In summary, we have developed template-assisted method to prepare the ordered mesoporous carbon supported CoFe species (CoFe/NC) as highly efficient ORR catalysts. The optimized temperature ensures the successfully fabrication of the ordered mesoporous carbon and co-existence of dual metal atoms/alloys. The ordered mesoporous structure promotes the

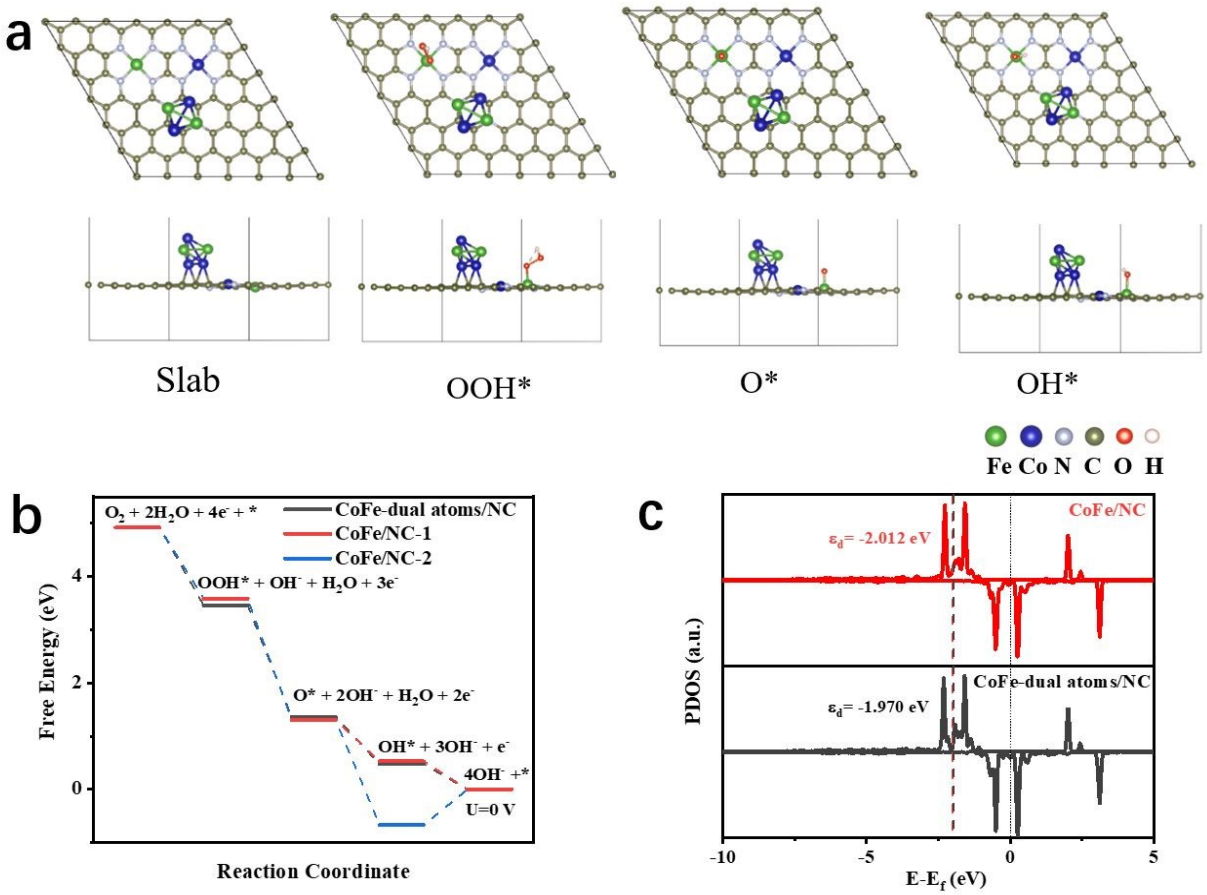

Fig. 4 DFT calculation results of CoFe/NC-750. (a) The reaction scheme with the intermediates in the ORR process on CoFe/NC.(b) Free-energy paths of ORR intermediates on CoFe-dual atoms/NC, CoFe/NC-1 and CoFe/NC-2. (c) The PDOS of d orbitals of active Fe atoms on CoFe/NC and CoFe-dual atoms/NC.

mass/charge transfer and the synergistic effect of CoFe bimetallic species modulates the active sites for boosted ORR. The CoFe/NC-750 exhibits excellent ORR performance with high $E_{1/2}$ of 0.87 V vs. RHE in 0.1 M KOH, no obvious attenuation after 3,000 cycles, which is superior to that of commercial Pt/C. The DFT calculation illustrated that the superior ORR performance originated from the electronic structure modulation of the catalytic active sites (atomically dispersed Fe sites) by CoFe alloy nanoparticles, which accelerates the dissociation and reduction of OH* and promotes the ORR process. Therefore, this study provides a promising strategy for designing highly efficient electrocatalysts for boosting the ORR process and the other energy conversion applications.

Conflicts of interest

The authors declare no conflict of interest.

Acknowledgements

Y. Z. acknowledges the support from the National Natural Science Foundation of China (22209103). All authors thank the support from the "Joint International Laboratory on Environmental and Energy Frontier Materials" and "Innovation Research Team of High-Level Local Universities in Shanghai". H.L. thanks the financial support from Australian Research Council (FT180100705) and the support from CSIRO "International Hydrogen Research Collaboration Program-RESEARCH FELLOWSHIPS". J. Z. thanks the support from UTS Chancellor's Research Fellowships.

References

1 X. Tian, X. F. Lu, B. Y. Xia and X. W. Lou, *Joule*, 2020, 4, 45-68.
2 D. U. Lee, J.-Y. Choi, K. Feng, H. W. Park and Z. Chen, *Adv. Funct. Mater.*, 2014, 4.
3 X. Wang, Z. Li, Y. Qu, T. Yuan, W. Wang, Y. Wu and Y. Li, *Chem*, 2019, 5, 1486-1511.
4 Roger, M. A. Shipman and M. D. Symes, *Nat Rev Chem*, 2017, 1.
5 X. Cao, J. Huo, L. Li, J. Qu, Y. Zhao, W. Chen, C. Liu, H. Liu and G. Wang, *Adv.d Energy Mater.*, 2022, 12, 2202119.
6 S. D. Bhoyate, J. Kim, F. M. de Souza, J. Lin, E. Lee, A. Kumar and R. K. Gupta, *Coordin Chem Rev*, 2023, 474.
7 Z. F. Huang, J. Wang, Y. Peng, C. Y. Jung, A. Fisher and X. Wang, *Adv.d Energy Mater.*, 2017, 7.
8 D. Zhao, Z. Zhuang, X. Cao, C. Zhang, Q. Peng, C. Chen and Y. Li, *Chem Soc Rev*, 2020, 49, 2215-2264.

9 J. Zhang, Y. Zhao, C. Chen, Y. C. Huang, C. L. Dong, C. J. Chen, R. S. Liu, C. Wang, K. Yan, Y. Li and G. Wang, *J Am Chem Soc*, 2019, 141, 20118-20126.
10 J. Huo, Z. Shen, X. Cao, L. Li, Y. Zhao, H. Liu and G. Wang, *Small*, 2022, 18, e2202394.
11 J. Huo, X. Cao, Y. Tian, L. Li, J. Qu, Y. Xie, X. Nie, Y. Zhao, J. Zhang and H. Liu, *Nanoscale*, 2023, 15, 5448-5457.
12 Q. Li, W. Chen, H. Xiao, Y. Gong, Z. Li, L. Zheng, X. Zheng, W. Yan, W. C. Cheong, R. Shen, N. Fu, L. Gu, Z. Zhuang, C. Chen, D. Wang, Q. Peng, J. Li and Y. Li, *Adv Mater*, 2018, 30, e1800588.
13 Y. Zhao, Z. Shen, J. Huo, X. Cao, P. Ou, J. Qu, X. Nie, J. Zhang, M. Wu, G. Wang and H. Liu, *Angew Chem Int Ed Engl*, 2023, 62.
14 Y. Tan, Z. Zhang, Z. Lei, L. Yu, W. Wu, Z. Wang and N. Cheng, *Appl. Catal. B Environ.*, 2022, 304.
15 H. Shang, X. Zhou, J. Dong, A. Li, X. Zhao, Q. Liu, Y. Lin, J. Pei, Z. Li, Z. Jiang, D. Zhou, L. Zheng, Y. Wang, J. Zhou, Z. Yang, R. Cao, R. Sarangi, T. Sun, X. Yang, X. Zheng, W. Yan, Z. Zhuang, J. Li, W. Chen, D. Wang, J. Zhang and Y. Li, *Nat Commun*, 2020, 11, 3049.
16 Y. Zhou, R. Lu, X. Tao, Z. Qiu, G. Chen, J. Yang, Y. Zhao, X. Feng and K. Mullen, *J Am Chem Soc*, 2023, 145, 3647-3655.
17 H. Xu, D. Cheng, D. Cao and X. C. Zeng, *Nat. Catal.*, 2018, 1, 339-348.
18 H. Peng, F. Liu, X. Liu, S. Liao, C. You, X. Tian, H. Nan, F. Luo, H. Song, Z. Fu and P. Huang, *ACS Catal.*, 2014, 4, 3797-3805.
19 L. Osmieri, A. H. A. Monteverde Videla, P. Ocón and S. Specchia, *J Phys Chem C*, 2017, 121, 17796-17817.
20 X. Ao, W. Zhang, Z. Li, J. G. Li, L. Soule, X. Huang, W. H. Chiang, H. M. Chen, C. Wang, M. Liu and X. C. Zeng, *ACS Nano*, 2019, 13, 11853-11862.
21 H. Huang, D. Yu, F. Hu, S. C. Huang, J. Song, H. Y. Chen, L. L. Li and S. Peng, *Angew Chem Int Ed Engl*, 2022, 61, e202116068.
22 J. Guo, J. Huo, Y. Liu, W. Wu, Y. Wang, M. Wu, H. Liu and G. Wang, *Small Methods*, 2019, 3, 1900159.
23 Y. Cheng, H. Song, J. Yu, J. Chang, G. I. N. Waterhouse, Z. Tang, B. Yang and S. Lu, *Chinese J Catal*, 2022, 43, 2443-2452.
24 C. Xu, C. Guo, J. Liu, B. Hu, J. Dai, M. Wang, R. Jin, Z. Luo, H. Li and C. Chen, *Energy Storage Mater*, 2022, 51, 149-158.
25 Z. Wang, C. Zhu, H. Tan, J. Liu, L. Xu, Y. Zhang, Y. Liu, X. Zou, Z. Liu and X. Lu, *Adv. Funct. Mater.*, 2021, 31.
26 S. H. Yin, J. Yang, Y. Han, G. Li, L. Y. Wan, Y. H. Chen, C. Chen, X. M. Qu, Y. X. Jiang and S. G. Sun, *Angew Chem Int Ed Engl*, 2020, 59, 21976-21979.
27 S. N. Zhao, J. K. Li, R. Wang, J. Cai and S. Q. Zang, *Adv Mater*, 2022, 34, e2107291.
28 Y. Li, H. Huang, S. Chen, X. Yu, C. Wang and T. Ma, *Nano Res*, 2019, 12, 2774-2780.
29 S. Hu, W. Ni, D. Yang, C. Ma, J. Zhang, J. Duan, Y. Gao and S. Zhang, *Carbon*, 2020, 162, 245-255.
30 S. Saifi, G. Dey, J. Karthikeyan, R. Kumar, D. Bhattacharyya, A. S. K. Sinha and A. Aijaz, *Inorg Chem*, 2023, 62, 8200-8209.
31 Y. Pan, X. Ma, M. Wang, X. Yang, S. Liu, H. C. Chen, Z. Zhuang, Y. Zhang, W. C. Cheong, C. Zhang, X. Cao, R. Shen, Q. Xu, W. Zhu, Y. Liu, X. Wang, X. Zhang, W. Yan, J. Li, H. M. Chen, C. Chen and Y. Li, *Adv Mater*, 2022, 34, e2203621.
32 L. Zhang, J. M. T. A. Fischer, Y. Jia, X. Yan, W. Xu, X. Wang, J. Chen, D. Yang, H. Liu, L. Zhuang, M. Hankel, D. J. Searles, K. Huang, S. Feng, C. L. Brown and X. Yao, *J Am Chem Soc*, 2018, 140, 10757-10763.
33 K. Kim, K. Min, Y. Go, Y. Lee, S. E. Shim, D. Lim and S.-H. Baeck, *Appl. Catal. B Environ.*, 2022, 315.
34 X. Cheng, Y. Wang, Y. Lu, L. Zheng, S. Sun, H. Li, G. Chen and J. Zhang, *Appl. Catal. B Environ.*, 2022, 306.
35 X. Duan, W. Tian, H. Zhang, H. Sun, Z. Ao, Z. Shao and S. Wang, *ACS Catal.*, 2019, 9, 7494-7519.
36 K. Wang, C. Qiu, Z. Wang, Q. Chen, J. Pan, J. Li, M. Wu, H. Dong, K. Shi and Q. Liu, *Carbon*, 2023, 214.
37 L. Song, J. Zhang, S. Sarkar, C. Zhao, Z. Wang, C. Huang, L. Yan and Y. Zhao, *Chem. Eng. J.*, 2022, 433.
38 T. Marshall-Roth, N. J. Libretto, A. T. Wrobel, K. J. Anderton, M. L. Pegis, N. D. Ricke, T. V. Voorhis, J. T. Miller and Y. Surendranath, *Nat Commun*, 2020, 11, 5283.
39 W. Xue, Q. Zhou, X. Cui, J. Zhang, S. Zuo, F. Mo, J. Jiang, X. Zhu and Z. Lin, *Angew Chem Int Ed Engl*, 2023, 62, e202307504.
40 S. Wei, A. Li, J. C. Liu, Z. Li, W. Chen, Y. Gong, Q. Zhang, W. C. Cheong, Y. Wang, L. Zheng, H. Xiao, C. Chen, D. Wang, Q. Peng, L. Gu, X. Han, J. Li and Y. Li, *Nat Nanotechnol*, 2018, 13, 856-861.
41 F. Shi, K. Zhu, X. Li, E. Wang, X. Zhu and W. Yang, *J Energy Chem*, 2021, 61, 327-335.
42 W. Zhang, Y. P. Chen, L. Zhang, J. J. Feng, X. S. Li and A. J. Wang, *J Colloid Interface Sci*, 2022, 626, 653-661.
43 X. Guo, W. Zhang, J. Shi, M. Duan, S. Liu, J. Zhang, Y. Liu, S. Xiong and Q. Kong, *Nano Res*, 2021, 15, 2092-2103.
44 X. Guo, J. Shi, M. Li, J. Zhang, X. Zheng, Y. Liu, B. Xi, X. An, Z. Duan, Q. Fan, F. Gao and S. Xiong, *Angew Chem Int Ed Engl*, 2023,62, e202314124.
45 T. Tang, Y. Wang, J. Han, Q. Zhang, X. Bai, X. Niu, Z. Wang and J. Guan, *Chin. J. Catal.*, 2023, 46, 48-55.